Review

Measurements and prediction of extreme defect distributions for fatigue assessment in multi-pass weld of 13%Cr–4%Ni alloy for hydraulic turbines

A. D'Andrea [a,*], M. Gagnon [b], S. Beretta [c,d], P. Bocher [a]

[a] École de technologie supérieure, 1100 Notre-Dame St W, Montréal, Québec H3C 1K3, Canada
[b] Institut de recherche d'Hydro-Québec (IREQ), 1800 Bd Lionel-Boulet, Varennes, QC J3X 1S1, Canada
[c] Politecnico di Milano, Department of Mechanical Engineering, via La Masa 1, 20156 Milano, Italy
[d] Auburn University, National Center for Additive Manufacturing Excellence, Department of Mechanical Engineering, Auburn, AL 36849, United States of America

ARTICLE INFO

ABSTRACT

Flux cored arc welding (FCAW) is a manufacturing process commonly used for hydro-turbine application, especially in the assembly of Francis runners made of 13%Cr–4%Ni stainless steel. The welded connection between the blade and band/crown is particularly susceptible to high stress levels due to the design of the runner and the presence of welding defects which act as localized stress concentrations. This research aims to predict the effect of these defects on the performance of the runner during operating condition. To investigate the occurrence of the defects, the distributions of the observed discontinuity are measured and analyzed on T-shape joint specimens using metallographic and X-ray 2D images. The data obtained from these two methods of acquisition are compared to identify any discrepancy. Extreme Value Statistic (EVS) is used to estimate the likely occurrence of the largest defects within the welded runner zone. Based on these findings, a probabilistic Kitagawa–Takahashi diagram with the El-Haddad approximation is adopted to quantify the influence of the defects size in the fatigue assessment.

Contents

---

* Corresponding author.
  E-mail address: antonio.dandrea.1@ens.etsmtl.ca (A. D'Andrea).

Nomenclature

Abbreviations

µ-CT	Micro-Computed Tomography
AM	Additive Manufacturing
AR	Aspect Ratio
Circ	Circularity
BM	Block Maxima
c.d.f	Cumulative distribution function
EVS	Extreme Values Statistics
FCAW	Flux Cored Arc Welding
HSV	Highly Stressed Volume
KT	Kitagawa–Takahashi
MLE	Maximum Likelihood Estimation
p.d.f.	Probability distribution function
SIF	Stress Intensity Factor

Symbols

$\hat{\delta}$	Scale parameter
$\hat{\lambda}$	Location parameter
$\hat{\xi}$	Shape parameter
$\Delta K_{th,LC}$	Long cracks threshold SIF range
$\Delta\sigma_{w0}$	Fatigue limit stress range defects-free
$\Delta\sigma_w$	Fatigue limit stress range
ϵ_f	Elongation at fracture
σ_{UTS}	Ultimate tensile stress
$\sigma_{y,0.2\%}$	Yield strength (offset 0.2%)
$\sqrt{area}$	Square root area of defect
F_{risk}	c.d.f. of Competing risk distribution
GEV	c.d.f. of GEV distribution
G	c.d.f. of Gumbel distribution
S_0	Surface area BM
S_1	Surface area BM (full weld)
V_0	Investigated volume BM
V_1	Investigated volume BM (full weld)
$V_{HSV}^{80\%}$	Highly Stressed Volume at blade hot-spot
$\tilde{\xi}$	Upper bound shape parameter
$\underline{\xi}$	Lower bound shape parameter
F	Cumulative frequency
R	Load ratio $\sigma_{min}/\sigma_{max}$
T	Return period
x	Generic random variable
Y	Murakami boundary correction factor

1. Introduction

Martensite stainless steel containing 13%Cr–4%Ni is commonly used to produce large Francis hydraulic turbine runners because of its excellent resistance to corrosion and cavitation erosion [1]. In a real turbine runner, as represented schematically in Fig. 1(b) for medium head geometry, the most critical region is the welded zone where the blade-band and blade-crown interface converge, specifically around the trailing edge, as reported in [2–4]. The design and the existence of welding defects make the volume of material in these zones susceptible to high stress levels, especially at the "hotspots" location, highlighted in red in Fig. 1(c). Given the thickness of the region that needs to be assembled, flux cored arc welding (FCAW) represents an efficient and productive method to perform high-volume material deposition. However, FCAW wire electrodes contain a flux core composed of
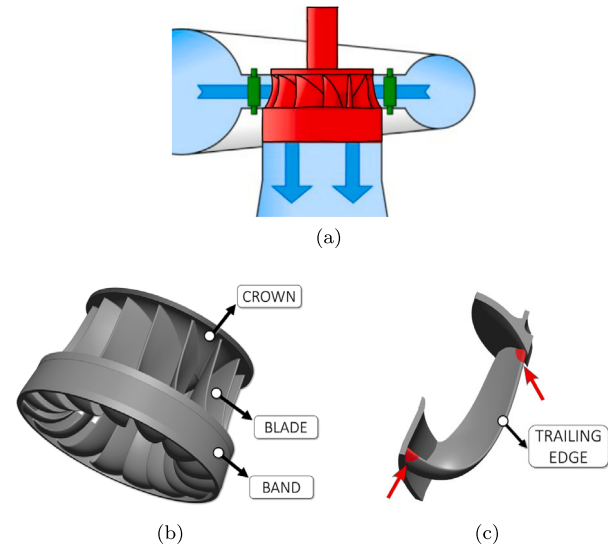

Fig. 1. Representation of (a) Francis turbine; (b) medium head Francis runner geometry and (c) blade geometry detail highlighting the high stress level zones ("hotspots" locations).

several metallic and non-metallic compounds (oxides of silicon, titanium, zirconium, etc.), that might get entrapped during the multi-pass welding procedure, creating inclusions [5]. Moreover, various welding discontinuities originated from other sources (gas porosity or lack of fusion) will also influence the material resistance during the cyclic load. As a consequence, different sources of heterogeneity in the material can act as crack nucleation sites.

Several studies in the literature have made efforts to identify discontinuities within multi-pass FCAW metal. Boukani et al. [5] have performed an investigation on Not-Destructive Testing (NDT) where slag welding inclusions were reported as expected. Similarly, Bajgholi et al. [6] have used Ultrasonic Testing (UT) to prove and generate a probability of occurrence of similar welding defects.

Even though previous failure investigations have shown that crack could initiate around material defects and affect the crack propagation, there is a limited research on the influence of defects on fatigue behavior for these materials [7]. Nowadays, the influence of defects on fatigue performance still remains a challenge to mitigate and multiple studies have emphasized the importance of addressing the impact of defects during the design process [8,9]. Therefore, the characterization of defects is primarily important when a defective component is subjected to a cyclic load.

In the world of design and manufacturing, reliability is a paramount concern. Ensuring the reliability of a component involves the understanding of the statistical probability of its fracture event, which is related to the probability of finding a weak point in the material microstructure (e.g., porosity or inclusion). The simplest probabilistic model to describe such effect is the concept of the weakest link (WL), widely adopted in literature to compute probabilistic fatigue assessment for component containing defects [10]. In the context of Francis runners, Gagnon et al. [11] have used such probabilistic fatigue assessment to test the fatigue reliability considering the distribution of typical defects. Defect analysis for other applications were also conducted by Romano et al. [12], which used a statistical approach known as "Extreme Value Statistics" (EVS) to perform a probabilistic fatigue assessment [13,14]. The concept of EVS applied to defects was initially introduced by Murakami to study the effects of small inclusions on fatigue strength. In this study, the fatigue assessment was computed by experimental formulations based on defect size measurements. The dimension of the defects was quantified by $\sqrt{area}$ parameter representing the square root of the measured inclusion area [15]. Most of
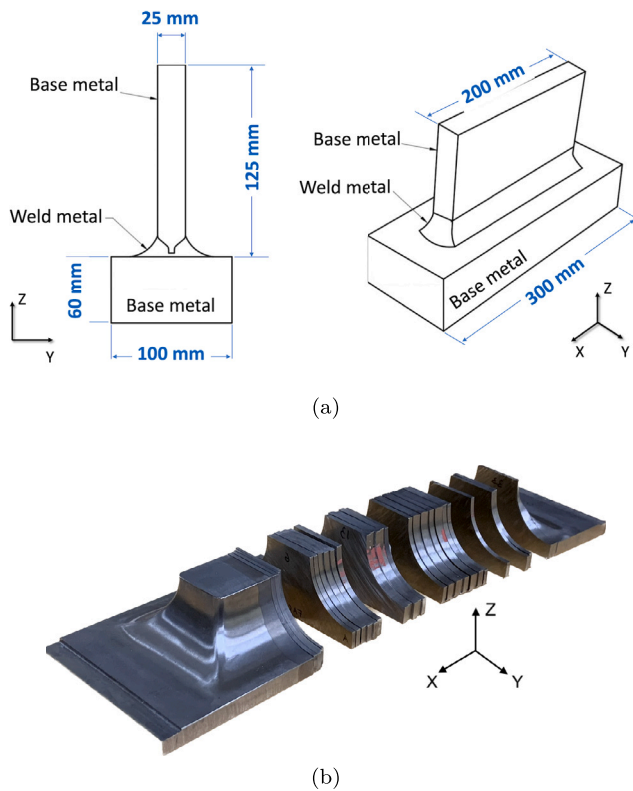
Fig. 2. Image of the T-shape welded joint: (a) geometry and (b) cross-section slices.

Table 1

Chemical compositions of 13%Cr–4%Ni alloys: CA6NM (ASTM A743) and 410NiMo (As measured) (wt%).

Material	Cr	Ni	Mo	C	Mn	Si	P	S
CA6NM	11.5–14	3.5–4.5	0.4–1	<0.06	<0.5	<0.1	<0.04	0.03
410NiMo	11.7	5.32	0.66	0.025	0.34	0.51	0.008	0.01

Table 2

Tensile properties of welded metal 410NiMo after post welded tempering treatment (PWHT) at 610($\pm$5) °C for 8 h.

Material	$\sigma_{y,0.02\%}$ [MPa]	σ_{UTS} [MPa]	ϵ_f [%]
410NiMo	681 $\pm$ 25	826 $\pm$ 27	11 $\pm$ 03

Table 3

Long crack thresholds stress intensity factor (SIF) range for 13%Cr–4%Ni stainless steels.

R	0.7	0.05	−1
$\Delta K_{th,LC}$ [MPa $\sqrt{m}$]	2.24 [22]	5.37 [22]	11.00 [23,24]

2.1. Material and welding parameters

The material under investigation is a martensite 13%Cr–4%Ni metal cored wire (410NiMo), welded on a base metal CA6NM (ASTM A743). The chemical nominal compositions of the base and welded metals are indicated in Table 1.

The welded region includes about thirty weld beads of 410NiMo material deposited using a FCAW in semi-automatic configuration. The welder was manipulating the welding gun while the electrode was automatically fed to the arc. The welding parameters used to manufacture the T-shape welded joint represent typical manufacturing conditions for Francis runners, and they are reported in Table 4. A post welded tempering treatment (PWHT) at 610($\pm$5) °C for 8 h was performed, with air as cooling medium without convection. This solution generates a significant decrease in residual stress [20] with a well characterized microstructure [21]. In this study, the residual stresses were low and thus not included in the analysis below. The heterogeneity in the microstructure of the weld was not considered, in accordance with the hypothesis of Linear Elastic Fracture Mechanics (LEFM). In this condition, the microstructure consists of some tempered martensite and about 17% of reformed austenite [21].

The mechanical properties of 410NiMo welded metal are reported in Tables 2 and 3. The tensile properties of welded metal 410NiMo were computed with a tensile test performed according ASTM E8 whereas the long crack thresholds stress intensity factor (SIF) range were obtained from literature [22–24].

The T-joint was cut with an abrasive cutting machine in 34 cross-section slices (Z–Y plane) with similar thickness (3 mm). Six of them were selected randomly and used to extract the data necessary for the analysis of the defects. The region of interest was focused on the welded material 410NiMo in the Z–Y plane (see Fig. 2(a)).
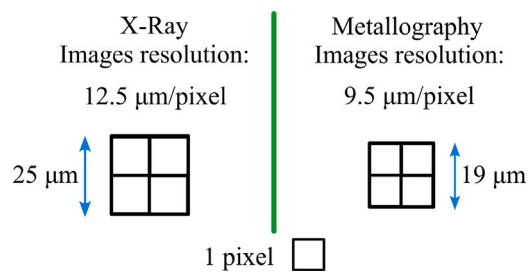
2.2. Method of acquisition

The acquisition of defects was conducted on 3 mm thick cross-section slices using X-ray 2D scans and metallographic macro-graphs. The choice of 3 mm thickness was a compromise to detect defects with acceptable contrast in X-ray. The shape of the slices have prevented the use μ-CT scanning, a common method for 3D defect analysis, widely documented in the literature. The two methods have different image resolutions: 1 pixel in X-ray radiography is 12.5 μm whereas in metallography images 1 pixel is 9.5 μm.

A threshold detection limit was set for the minimum defect size which was chosen as twice the resolution of the corresponding technique of acquisition, as illustrated in Fig. 3. This criterion was implemented to ensure that observations with a resolution of only one

these concepts are recently applied to additive manufacturing (AM) fatigue assessment for structural part highlighting the impact of defects in fatigue performance [10].

In literature, the Kitagawa–Takahashi (KT) diagram is often adopted to establish a correlation between the distribution of the identified defects and the fatigue performance [16]. This diagram combines the concept of fatigue crack growth threshold and the fatigue endurance limit into a single plot, relating the size of defects and the endurance limit. It defines a transition zone from short to long crack propagation regime. This approach is commonly employed in fracture mechanics design of components and fracture control, such as the fail-safe principle [17–19].

In this contest, the paper aims at presenting a methodology to document the impact of defects in multi-pass welded material made of martensite stainless steel. Defects are measured on large T-shape joint specimens representative of Francis runners and analyzed with EVS statistics for fatigue assessment. The distributions of the expected defects rely on 2D measurements of the welded zone using radiography (as in the industry) and metallography images. The defects are characterized in terms of defect size ($\sqrt{area}$). Additional parameters such as circularity and aspect ratio (AR) are used to better describe the defect statistical behavior and estimate the size controlling the fatigue endurance limit before running any experimental fatigue tests.

2. Material and methods

The blade-band and blade-crown geometry were simplified to a T-shape welded joint manufactured in agreement with the common welding process used in Francis runner production to generate equivalent defects. Fig. 2 shows the specimen geometry 2(a) and an image of the welded part cut in cross-sections for the analysis 2(b).

Table 4
Welding parameters of T-shape welded joint.

Process	Shielding gas	Wire diameter [mm]	Current [A]	Voltage [V]	Torch speed [cm/min]	Distance [mm]	Pre-heating Temperature [°C]	Interpass Temperature [°C]
FCAW	75%Ar–25%CO2	1.6	245	26	30	20	120	170

Fig. 3. Minimum size of the acquired defects: 25 μm for X-ray and 19 μm for metallography.

Table 5
X-ray set up parameters.

Voltage	Current	Exposure time	Resolution
180 kV	80 μA	708 ms	12.5 μm/pixel

pixel (possibly noise) were not mistakenly considered as defects. As a consequence, the smallest defect size documented by the X-ray and metallography method was $\sqrt{\text{area}} = 25$ μm and $\sqrt{\text{area}} = 19$ μm, respectively.

X-ray 2D scan provides the capability to project to a plane the entire volume of the material and likely the various population of defects (e.g. pores, voids, inclusions, etc.), whereas metallography is limited to a single plane of observation, limiting the detection of the defects. In both cases, the plane of observation does not necessarily coincide with the plane of the largest cross-section of the defect. For instance, defect sizes determined with X-ray could have smaller size in the Y-Z plane of observation, but more elongated along the X dimension. This is a type of underestimation that characterizes data coming from X-ray acquisitions, as illustrated in Fig. 4(a). Similarly, in the plane of observation for metallography the maximum defect size is not precisely the truth maximum size of the defect, as illustrated in Fig. 4(b). Although widely used for defect analysis, metallography has its limitations, which have been extensively recognized in the literature, as discussed [25,26]. Despite these, metallographic macro-graphs are widely used in the industry for root cause analysis due to their simplicity and ability to provide quick qualitative analysis [27,28]. They offer a unique perspective, revealing structural details and defects often invisible to other techniques like ultrasonic testing or radiography. This capability allows for the identification of grain boundaries, phase distributions, and microstructural anomalies, providing insights that other methods cannot match. For this reason, this method was used and compared with X-ray technique.

2.2.1. X-ray

The X-ray 2D scans of the welded material were achieved by Nikon XT-H-225. Each cross-section slice was divided in 3 regions to reach the highest-resolution possible. The X-ray set up parameters are reported in Table 5 and each acquired image was an average of 64 shootings.

Image processing was carried out using an auto-threshold method called "Otsu" in Fiji/ImageJ software. Otsu's method is an image processing technique used for automatic image thresholding. It works by finding the optimal intensity threshold that separates an image into the foreground and background. The method involves calculating the histogram, probability distribution, and cumulative distribution of pixel intensities. By maximizing the variance between foreground and background, Otsu's method determines the best threshold for creating a binary image, supporting tasks like image segmentation [29]. Therefore, this threshold method has facilitated the quantification of several parameters including defect size, circularity, and aspect ratio.

An example of post-processed image with highlighted detected defects is provided in Fig. 5(a). Most of the large observed discontinuities

are located at the top connection between welded and base metal, with the present of several clusters. A detailed view of a cluster of defects is shown in Fig. 5(c). X-ray results have also shown large internal defects at the root of the multi-passes welds, as indicated by the arrow in Fig. 5(a). These defects were not considered in this analysis because they are not correlated with those produced by the FCAW process, but rather related to areas of low accessibility.

2.2.2. Metallographic macro-graphs

Metallographic macro-graphs were performed on one side of the six selected cross-section slices. The chosen side was initially polished for the image acquisition to perform the defect analysis. The surface was prepared using an automatic Tegramin machine (Struers) with P320, P600 and P1200 SiC abrasive grinding papers followed by polishing with 9, 3, and 1 μm diamond suspension. To achieve a good compromise between quality and image resolution, a 50x magnification was set for the acquisition and images were automatically stitched together to reconstruct the entire cross-section slice. Image processing was also performed using the "Otsu" thresholding technique in Fiji/ImageJ to quantify defect size, circularity, and aspect ratio parameters. After the image acquisition, on the same polished surface a chemical etching with Vilella's reagent was used to reveal the martensite microstructure and welded passes [30]. The revealed microstructure is consistent with the findings of M.M. Amrei et al. [31], where fine e columnar microstructure were reported. A detailed view in Fig. 5(d) highlights the main feature of the microstructure and the defects dimensions. Fig. 5(b) corresponds to the same slice of Fig. 5(a) and it shows the metallographic macro-graph obtained by combining surface polishing and surface etching together. Thanks to this combination, it was possible to highlight the weld beads and to clearly show the defects across the region of interest.

2.3. Defect analysis strategy

2.3.1. Classification of defects

The defects of the entire welded 410NiMo region were compared in terms of defect size, aspect ratio (AR) and circularity. The location of the defect due to the complex T-shape slice geometry is simplified to the assumption that any defect not in contact with the free surface is considered internal. Due to the limited amount of material on the free surface of the T-shaped joint (3 mm thick slices), surface defects are few and not statistically treatable. Therefore, all defects are treated as internal in the analysis. The adopted defect size terminology is the $\sqrt{\text{area}}$ parameter and as mentioned in [15] it is usually represented by the square root of the measured inclusion area. The aspect ratio is a parameter that measures the elongation of a defect. This parameter is obtained by quantifying the ratio between the minor and major axes of the ellipse that is fitted to the original shape of the defect preserving its area. The expression of this ratio is defined by Eq. (1a) where minor axis is b and major axis is a and its value varies between 0 and 1 with lower values meaning more elongated defects. Circularity is another measure of the irregularity of a defect and it is calculated as the ratio between the equivalent and the real perimeter of the defect,
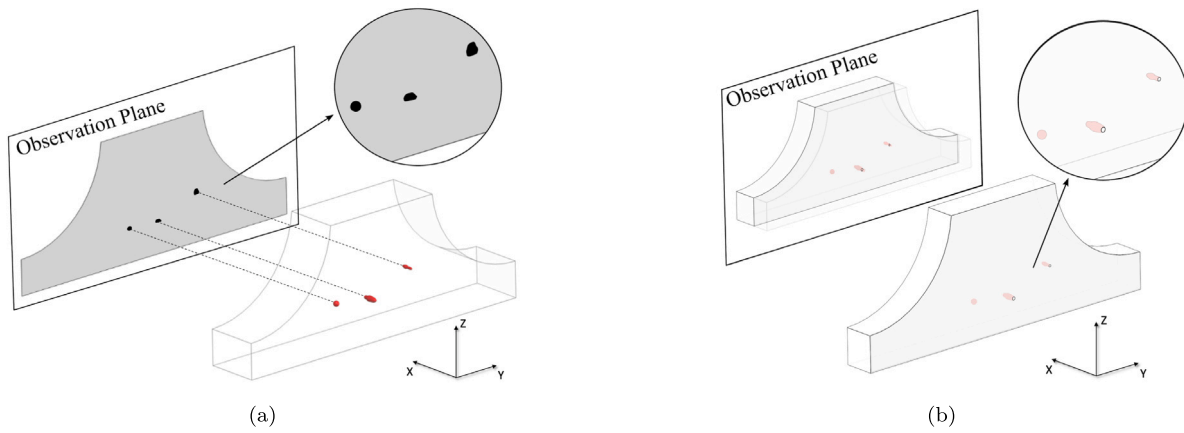
Fig. 4. Graphical descriptions showing the expected underestimation of defect size using (a) X-ray and (b) Metallography method of acquisition.
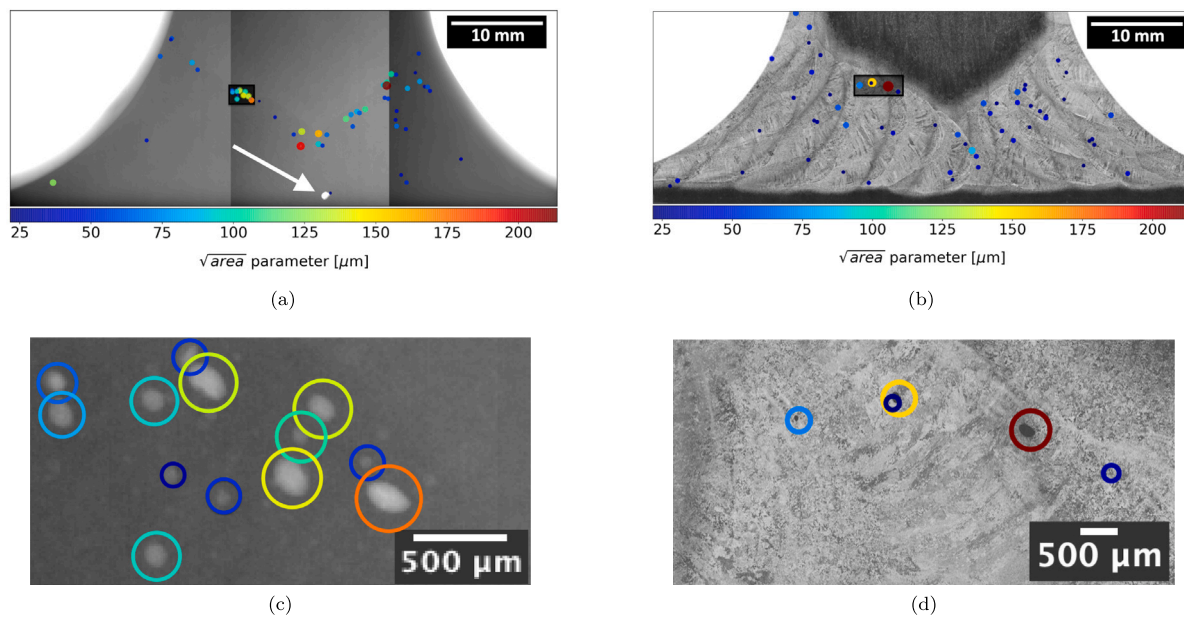

Fig. 5. Location and dimensions of the detected defects: (a) analysis from X-ray imaging; (b) analysis from metallography imaging; (c) detailed view of defect clusters identified via X-ray imaging; (d) detailed view of the microstructure and defects identified via metallography imaging. The scale bars in (c) and (d) are different. The color represents the size of the defect according to $\sqrt{area}$ parameter.

respectively expressed as P_{equiv} and P_{real} in Eq. (1b). In 2D analysis, circularity varies between 0 and 1 and a value of 1 represents a perfect circle, whereas values approaching 0 indicate an increasingly irregular shape [29]. Fig. 6(a) shows the graphical representations of these two defect irregularity parameters.

$$AR = \frac{b}{a} \tag{1a}$$

$$Circ = \frac{P_{equiv}}{P_{real}} = \frac{2 \cdot \sqrt{\pi A}}{P_{real}} \tag{1b}$$

The AR and circularity parameters of detected defects are shown in Fig. 7. Particularly, in Figs. 7(a) and 7(b) the aspect ratio and circularity of each defect are compared with the defect size and divided by method of acquisition: X-ray data in black and white (o) and metallography ones in red (+). Aspect ratio and circularity parameters are also displayed individually in terms of empirical cumulative distribution to highlight the frequency of the observed data, as illustrated in Figs. 7(c)–7(d). When acquired through the metallography method, numerous detected defects exhibit similar values of aspect ratio (∼0.68) and circularity (∼1), as shown by Figs. 7(c) and 7(d), respectively. This
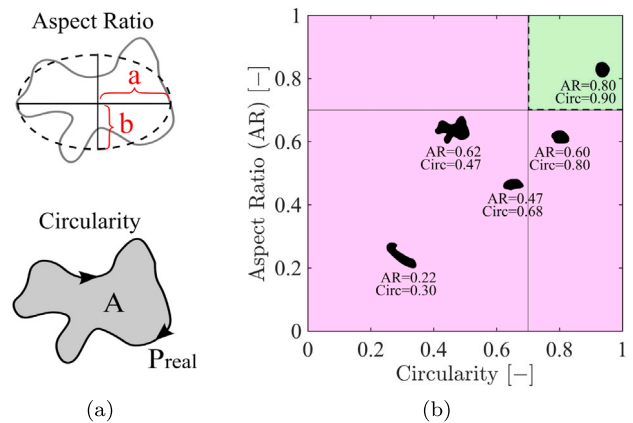

Fig. 6. Classification of the detected defects: (a) Graphical representations of aspect ratio and circularity; (b) Schematic diagram to classify defect morphology with examples of few detected defects.
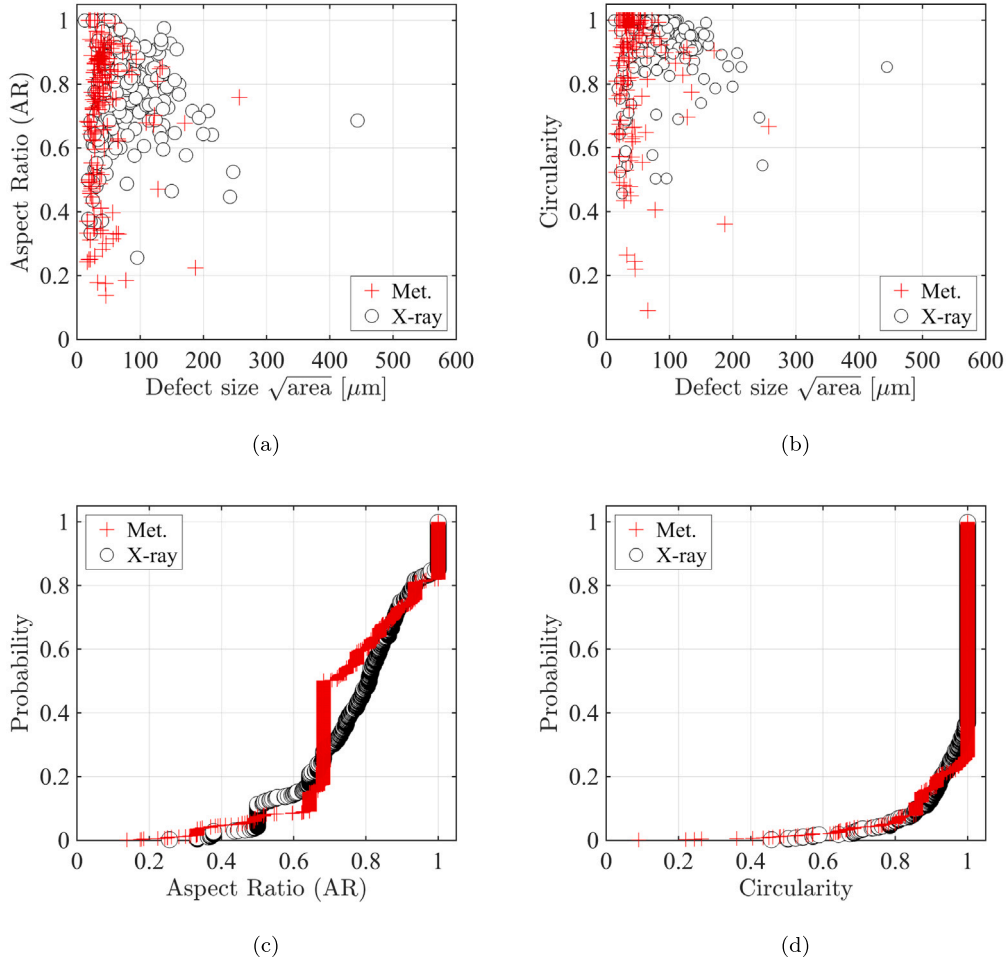
Fig. 7. Properties of detected defects according to Aspect ratio (AR), circularity and defect size parameter: (a) AR vs defects size; (b) circularity vs defects size; (c) empirical cumulative distribution for AR parameter; (d) empirical cumulative distribution for circularity parameter.

repetition of the same value is assumed to be attributed to the inherent characteristics of the acquisition method itself. On the contrary, detected defects acquired through the X-ray method show a smoother behavior.

Based on the analysis of the AR and circularity data, the defects were classified into two main categories: defects with AR and circularity >0.7 identified as "Spherical" discontinuity, and the remaining defects treated as "Elongated" discontinuity. The two categories are respectively displayed in Fig. 6(b) as green and magenta area. Sanaei et al. [32] have introduced a similar methodology to classify 2D observed discontinuities to characterize their variability in AM components. In the current study, the distribution of the observed defects was analyzed both as a unified distribution including spherical and elongated defects together, and additionally, the defects were also examined independently.

2.3.2. Statistical approach

The extreme values of the defect size obtained experimentally were modeled using the "Generalized Extreme Value" (GEV) distribution and its asymptotic formulations. The cumulative distribution function (c.d.f.) of GEV is expressed by Eq. (2), whereas c.d.f. of Gumbel distribution (asymptotic case) is expressed by Eq. (3).

$$\text{GEV}_{\hat{\xi},\hat{\lambda},\hat{\delta}}(x) = \exp\left\{-\left[1 + \hat{\xi}\left(\frac{x - \hat{\lambda}}{\hat{\delta}}\right)\right]^{-1/\hat{\xi}}\right\} \tag{2}$$

$$G_{\hat{\delta},\hat{\lambda}}(x) = \exp\left[-\exp\left(-\frac{x - \hat{\lambda}}{\hat{\delta}}\right)\right] \tag{3}$$

where $\hat{\lambda}$, $\hat{\delta}$ and $\hat{\xi}$ are the "location", "scale" and "shape" distribution parameters. The estimated location parameter $\hat{\lambda}$ is the modal value of the distribution shifting the probability density function (p.d.f.) to the right or to the left, $\hat{\delta}$ compresses or stretches the p.d.f. of the distribution, and $\hat{\xi}$ controls the shape of the distribution. Depending on the value of the estimated shape parameter $\hat{\xi}$ in Eq. (2), three possible asymptotic distributions are achievable: Fréchet distribution ($\hat{\xi} > 0$), Weibull distribution ($\hat{\xi} < 0$) and Gumbel distribution ($\hat{\xi} = 0$) [33]. The parameters of the distribution are calculated by Maximum Likelihood Estimation (MLE), which consists of maximizing the probability that sample data belong to the selected distribution [14]. Additionally, MLE has also given the estimation of the confidence intervals for these parameters. This becomes crucial as it provides a range of values within which the true parameters value can reasonably be expected to fall, offering a measure of the uncertainty associated with the estimate. The importance of the confidence intervals becomes evident in determining whether to apply an asymptotic distribution or not, particularly for the shape parameter $\hat{\xi}$. Indeed, if both confidence bounds are negative/positive, there is a statistical evidence suggesting that the estimated parameter will be negative/positive, whereas if the lower bound $\underline{\xi}$ is negative and the upper bound $\tilde{\xi}$ is positive, there is no statistical evidence favoring either a positive or negative value. In such cases, the value $\hat{\xi} = 0$ is chosen, simplifying the decision-making process and aligning with the asymptotic case corresponding to the Gumbel distribution represented by Eq. (3).

The dimensions of the largest inclusions were measured and analyzed, according to the block maxima (BM) sampling technique [13].
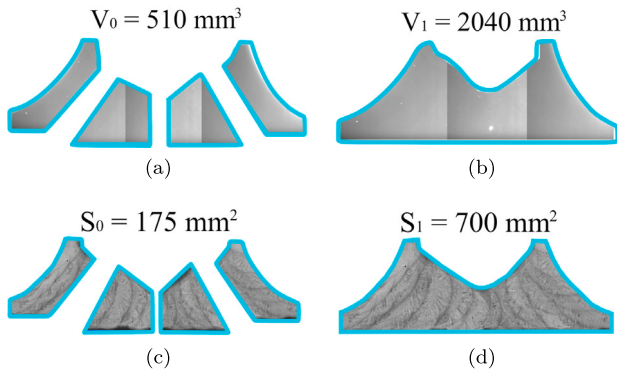
Fig. 8. Representation of sampling blocks in the case of a quarter of weld (a), (c) and full weld (b), (d).

Fig. 9. Flow chart of competing risk strategy applied to EVS.

According to the mentioned block maxima strategy, only the largest defects observed in the investigated volume were used for this statistical approach. In the analysis, two main block sampling sizes were selected: one representing a quarter of the welded region and the other including the entire welded region itself.

Fig. 8 illustrates the X-ray investigated volumes V_0 and V_1 and the corresponding surface area for metallographic macro-graphs S_0 and S_1, respectively. The investigated volume V_0 and V_1 were computed considering the actual volume analyzed by the radiography and used for the X-ray analysis. On the other hand, the surface areas S_0 and S_1 were adopted to obtain equivalent volumes necessary to compare metallographic results with those obtained from X-ray analysis. Murakami in [7,34] has proposed a methodology to predict larger inclusion size based on 2D metallography observations. The predicting method was based to assign a fictitious thickness h_0 to the surface area S_0. The fictitious thickness h_0 was computed considering the average value among the observed largest defect size in the different surface areas S_0. In this way, it was possible to determine an equivalent volume $(S_0 \cdot h_0)$ necessary to predict the largest inclusion within a target volume. In the present study, the number of surface areas S_0 and S_1 are 24 and 6, respectively. The average size of the largest defects observed on the surface areas were used as a fictitious thickness to calculate the equivalent volumes V_0^* and V_1^*. This approach offers the advantage of conducting a 3D analysis based on 2D measurements, but the associated volumes could be significantly different from the actual ones.

The use of extreme value statistics solely based on the full weld sampling blocks (see Fig. 8), providing only six defects in total, may not yield sufficiently robust results. Therefore, to avoid this, the researchers opted to perform the analysis on the smaller investigated volume, V_0, represented by a quarter of the full welded 410NiMo region (see Fig. 8). This adjustment aimed to enhance the reliability and accuracy of the analysis.

Firstly, the attention was centered on the distribution of all the defects which were fitted with a GEV and a Gumbel distribution and displayed on the Gumbel probability paper plot. On this probability plot, it is possible to illustrate the fitted cumulative distribution function and also the experimental data in terms of empirical cumulative probability.

Secondly, the defects were separated in the category mentioned in Section 2.3.1 and analyzed according to the extreme value statistics. Maxima defects acquired on V_0 were considered separately as maxima spherical discontinuity and as maxima elongated discontinuity. To examine the impact that each category of defects had in the overall distribution, spherical and elongated defects were fitted with a GEV distribution independently. Afterwards, the resulting estimated shape parameters and its confidence intervals were used to choose the proper asymptotic distribution [33]. At the end, the superimposition of the spherical and elongated fitted distributions was treated according to
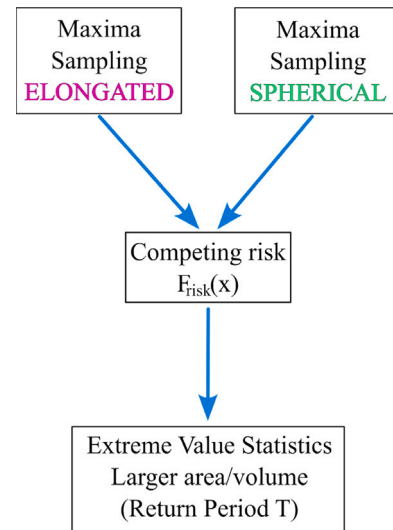
a competing risk approach, a strategy adopted by Beretta et al. [35] for the investigation of multiple particles effects. The entire process is schematically presented in Fig. 9 and the c.d.f. representing the competing risk distribution on the volume V_0 is expressed by the Eq. (4), assuming that it consists of a combination of a Gumbel and a GEV distribution.

$$F_{risk,V_0}(x) = G_{\hat{\delta},\hat{\lambda}}(x) \cdot GEV_{\hat{\xi},\hat{\delta},\hat{\lambda}}(x) \tag{4}$$

Once that the competing risk distribution is identified for the volume V_0, the statistics can be generalized to volumes larger than the investigated one using the concept of the "return period". For example, the expected distribution of the maximum defect on the volume V_1 can be obtained as:

$$F_{risk,V_1}(x) = \left[F_{risk,V_0}(x)\right]^T \tag{5}$$

where $T = V_1/V_0$ is the return period for the largest defects in V_1 when block maxima sampling is adopted [13,14].

The discussed volumes shown in Fig. 8 are simplified cases and not fully representative of the real application. For this reason, another volume was introduced to simulate the stressed volume at the hotspots of the Francis runner. Kuguel et al. [36] discussed that for any volume geometry, there is a portion of volume called Highly Stressed Volume (HSV) that is particularly critical when assessing the potential fatigue failure. After the introduction of this concept, the HSV was used by several authors [37,38] to determine the highly stressed volume in terms of a specific percentage of the maximum stress. Romano et al. [10] and Beretta et al. [39] have demonstrated that a portion of material subjected to a percentage between 95% and 80% of the maximum stress is significantly critical in terms of fatigue assessment, especially in presence of defects. In the present analysis, the highly stressed volume is represented by the volume subjected at least to 80% of the maximum principal stress at the hotspot and indicated as $V_{HSV}^{80\%}$. Finite element analysis is often used to identify crucial hotspots and their associated maximum principal stress, which is influenced by both the geometry of the Francis runner and the operating conditions of the turbine. In the case under study, $V_{HSV}^{80\%}$ was estimated for a medium head Francis turbine operating at maximum power with runner geometry similar to the one represented in Fig. 1(b). For instance, according to this case, the value of $V_{HSV}^{80\%}$ is 1700 mm^3 and the hotspot is located at the blade-band interface, as illustrated in Fig. 10 [40].
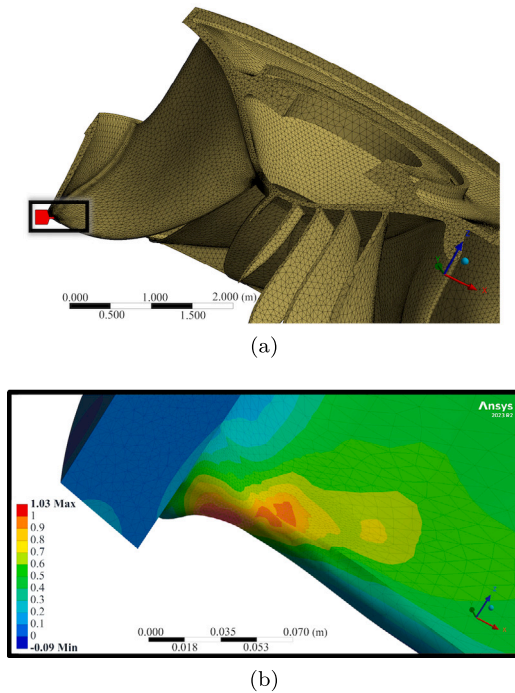
(a)

(b)

Fig. 10. Finite element analysis showing the highly stress volume for a medium head Francis runner operating at maximum power: (a) location of the hotspot; (b) normalized maximum principal stress to identify the $V_{HSV}^{80\%}$ (regions in orange and red).

2.3.3. Kitagawa-Takahashi diagram

The Kitagawa–Takahashi (KT) diagram is commonly used in literature to illustrate how the fatigue limit decreases with the increasing size of the defect [16]. This diagram represents a tool widely employed for fatigue assessment in various studies [17,19,41] and, in this study, it was used to estimate how the defect size ($\sqrt{\text{area}}$) affects the fatigue limit stress range ($\Delta\sigma_w$) representing the fatigue strength at 10 million cycles for infinite life. To simplify the investigation, the statistical approach was only implemented for infinite life avoiding any detailed analysis for finite life. Among different approaches, the modified El-Haddad formulation is particularly interesting because it describes a smooth transition from short to long cracks and it is controlled by the El-Haddad parameter ($\sqrt{\text{area}_0}$) expressed by Eq. (6a) [42].

$$\sqrt{\text{area}_0} = \frac{1}{\pi}\left(\frac{\Delta K_{th,LC}}{Y \cdot \Delta\sigma_{w0}}\right)^2 \tag{6a}$$

$$\Delta\sigma_w(\sqrt{\text{area}}) = \Delta\sigma_{w0} \cdot \sqrt{\frac{\sqrt{\text{area}_0}}{\sqrt{\text{area}} + \sqrt{\text{area}_0}}} \tag{6b}$$

In Eq. (6a) $\Delta K_{th,LC}$ represents the long crack threshold SIF range; $\Delta\sigma_{w0}$ is the fatigue limit stress range of the defect-free material [7] and Y is the Murakami's boundary correction factor [7,43]. In this study, Y is equal to 0.5 because internal defects are considered. Then Eq. (6b) corresponds to the analytical expression for the smooth short-long crack transition and it was used to determine the value of the fatigue limit stress range $\Delta\sigma_w$ for a specific defect size $\sqrt{\text{area}}$. In the present study, the variables used in the El-Haddad model ($\Delta K_{th,LC}$, $\Delta\sigma_{w0}$) are assumed to be perfectly correlated as stated in [44] to have a straightforward link between them.

The El-Haddad parameter is graphically represented in Fig. 11 and it corresponds to the intersection between the dashed red line defining the fatigue limit stress range of the defect-free material $\Delta\sigma_w = \Delta\sigma_{w0}$ and the solid red line computed by the long crack threshold SIF range $\Delta K_{th,LC}$ $\left(\Delta\sigma_w = \Delta K_{th,LC}/Y\sqrt{\pi\sqrt{\text{area}}}\right)$.
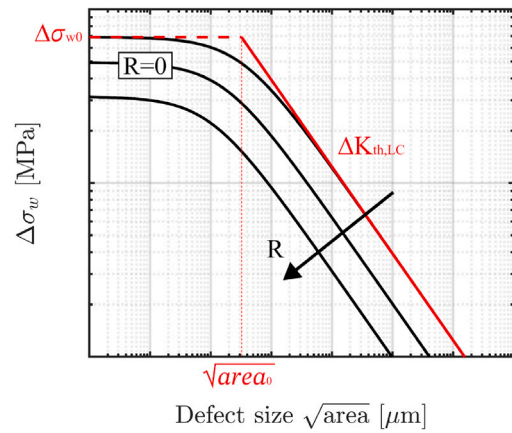

Fig. 11. Schematic Kitagawa–Takahashi diagram and its dependency on R.

The KT diagram varies with the load ratio R because the El-Haddad parameter depends on $\Delta\sigma_{w0}(R)$ and $\Delta K_{th,LC}(R)$, both a function of load ratio R. This modifies the asymptotic lines for each load ratio, leading to different $\Delta\sigma_w(R)$ curves as illustrated in Fig. 11. For this reason, for each load ratio R the material parameters $\Delta\sigma_{w0}(R)$ and $\Delta K_{th,LC}(R)$ are computed respectively by the Goodman equation as reported in Eq. (7) and by the long crack threshold SIF range data from experimental tests or NASGRO fitting [45].

$$\Delta\sigma_{w0}(R) = \frac{1}{\frac{1+R}{1-R} \cdot \frac{1}{\sigma_{UTS}} + \frac{1}{\Delta\sigma_{w0}^{R=-1}}} \tag{7}$$

3. Results & Discussion

In accordance with the detection defect procedure mentioned in Section 2.2, the number of observed defects and the absolute maximum defect size for the X-ray and metallography method of acquisition are reported in Table 6. For the same region of interest, the number of discontinuities identified by X-ray is found to be lower compared to those determined by metallographic macro-graphs, but the associated size is significantly larger.

The difference in the image resolutions of the two methods significantly affects the defect detection, as shown by Figs. 3 and 4. For this reason, X-ray data were analyzed in detail, as this method of acquisition provides a complete overview of the defects throughout the material. This is especially true when the focus is on the population of the largest discontinuities. The divergences between the two methods are examined at the end of Section 3.2, focusing on the estimation of the fatigue limit stress range ($\Delta\sigma_w$).

Table 6
Features of the detected defects in the 410NiMo welded material analyzing six T-shape cross-section slices.

Method of aquisition	Number of defects		Max defect size [μm]	
	Spherical	Elongated	Spherical	Elongated
X-ray	327	103	207	444
Metallography	337	131	135	257

3.1. Extreme values and defect analysis

The overall defects (spherical and elongated together), observed on the investigated volumes V_0, were analyzed according to GEV extreme statistics. The maximum likelihood estimation of the GEV distribution parameters have provided the estimates of the shape parameter $\hat{\xi}$ and its confidence intervals. The confidence interval values of the shape parameter ($\underline{\xi}, \bar{\xi}$) did not exclude the possibility to fit the X-ray data with
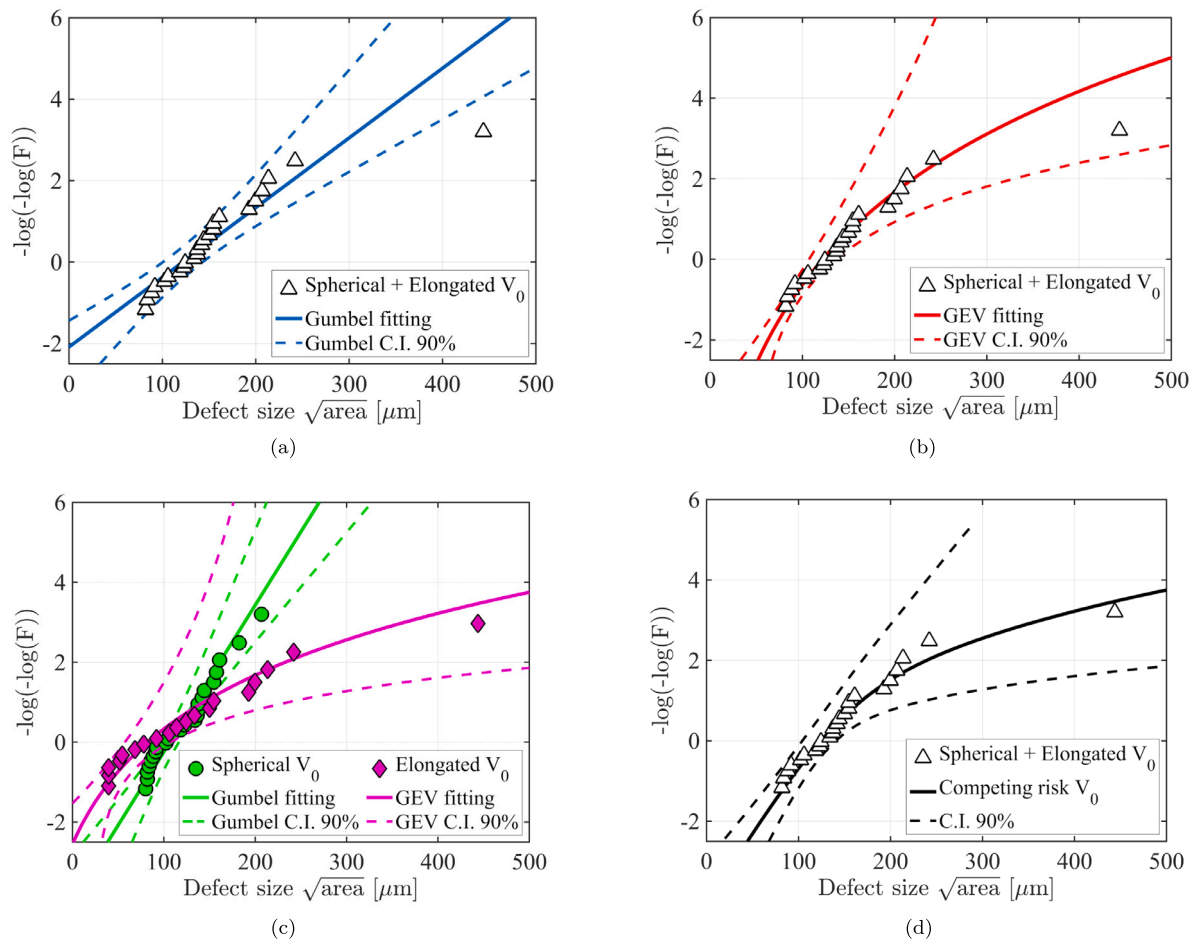
Fig. 12. Results of X-ray data on V_0: (a) Gumbel fitting of the overall observed defects; (b) GEV fitting of the overall observed defects; (c) extreme statistics applied to spherical and elongated category; (d) competing risk applied to the overall defects (Spherical+Elongated).

the Gumbel distribution ($\hat{\xi} = 0$). Therefore, Fig. 12(a) illustrates the Gumbel fitting on a Gumbel probability plot with the experimental observed defects and 90% confidence intervals. The Gumbel distribution fails at including all the largest defects, as the observed defect at 444 μm is out from the 90% confidence intervals. The GEV fitting with the associated 90% confidence intervals (Fig. 12(b)) shows an improvement as all the largest defects fall within the confidence intervals; however, it does not yet precisely represent the distribution of the largest sizes of defects. The inaccuracy of the fittings for the welded discontinuities might be attributed to the present of more than one population of defects.

The morphology of the defects is chosen as a criterion to create two populations of defects (spherical vs elongated category) and each category is analyzed and fitted with the best respective extreme statistics. Spherical defects are best fitted with a Gumbel distribution, while elongated defects follows a Fréchet distribution, as shown in Fig. 12(c). The separated fitting clearly illustrates that the largest defects are described by the elongated distribution better than the previous case when spherical and elongated discontinuities were fitted together. The maximum likelihood estimations of the mentioned distributions parameters are collected in Table 7 for control volume V_0.

In Fig. 12(c), it is clear that for small values of Gumbel cumulative frequency F (equivalent to small return period), spherical defects are the largest discontinuities, and they will be the ones controlling the fatigue performance of the material. On the other hand, when large volumes are considered (large values of F), elongated defects are the most critical ones. These results illustrate the importance of considering the right size of samples to perform the characterization of the defects:

Table 7
Maximum likelihood estimation of distribution parameters for control volume V_0 (X-ray).

Type of distribution	Fitting parameters		
	$\hat{\xi} \; \{\underline{\xi}, \; \bar{\xi}\}$ [–]	$\hat{\lambda}$ [μm]	$\hat{\delta}$ [μm]
Gumbel (Spher.+Elo.)	–	121.51	58.42
GEV (Spher.+Elo.)	0.25 {−0.06, 0.56}	121.91	37.75
Gumbel (Spherical)	–	108.71	27.92
Fréchet (Elongated)	0.38 {0.01, 0.94}	82.33	50.31
Competing risk	0.38	108.71 & 82.33	27.92 & 50.31

if an excessively small volume (sample size) is considered to investigate the material, the population of defects that would be characterized might not be the one that will drive the material fatigue performance in larger volumes, i.e., in the real part.

The separated investigation of the two populations of defects resulted into a 90% confidence intervals wider than the case when considering the defects as a single population, as seen by comparing Figs. 12(b) and 12(c). With this approach, the necessity to use two separated statistical distributions to predict the fatigue limit makes the process less straightforward, justifying the development of the competing risk approach. The resulting competing risk distribution, generated by merging the two computed distribution from spherical and elongated defects, is presented in Fig. 12(d) together with its 90% confidence intervals. For defect sizes smaller than 230 μm, both the GEV and competing risk distributions accurately predict the sizes of the defects, as shown by the accurate fitting between the solid lines (predicted defect size) and the observed discontinuities in Figs. 12(b)
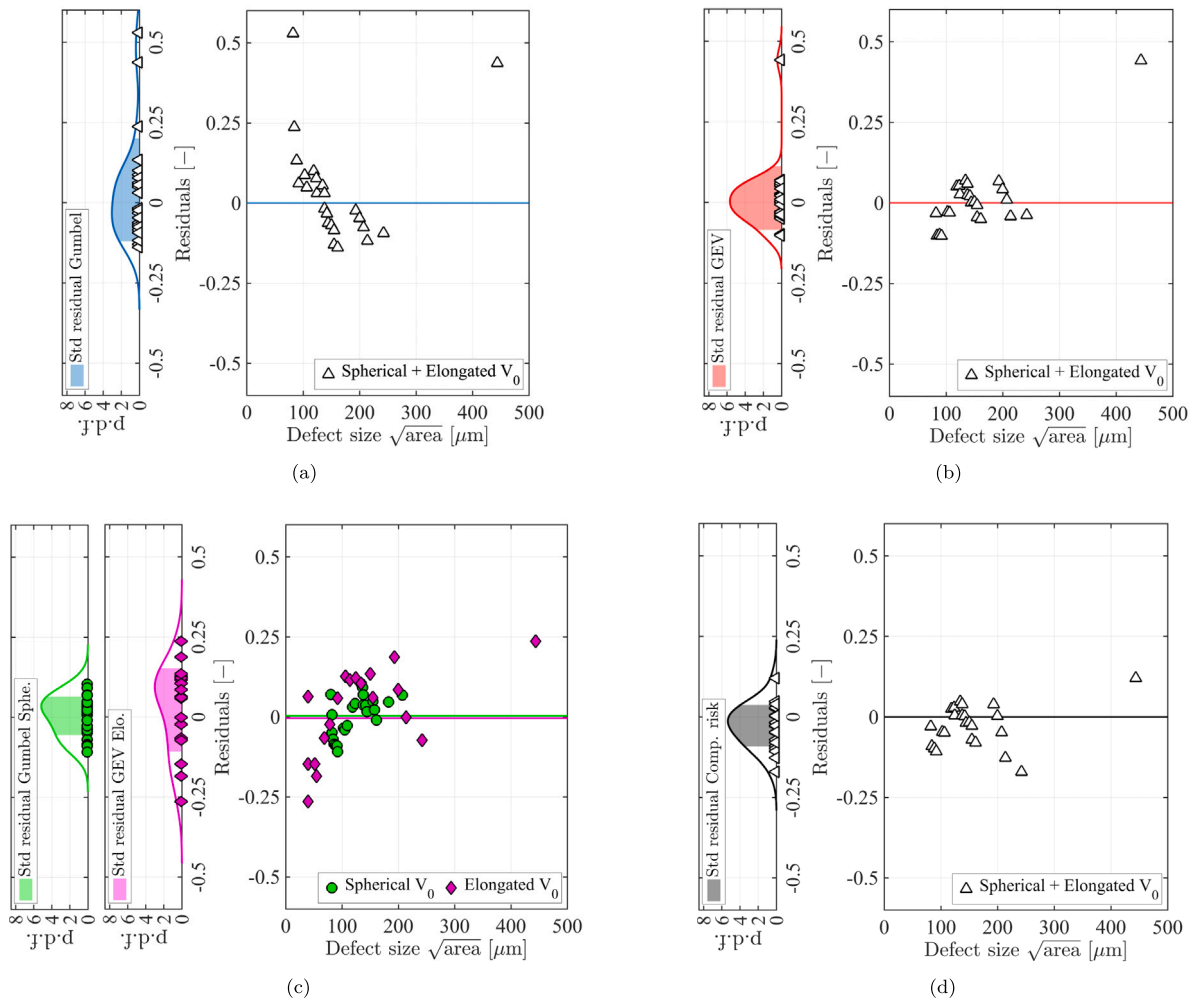
(a)

(b)

(c)

(d)

Fig. 13. Normalized residuals as a function of the defect sizes for the fittings achieved with the X-ray data on V_0: (a) Gumbel of the overall observed defects; (b) GEV of the overall observed defects; (c) Gumbel and GEV of spherical and elongated defects; (d) competing risk of the overall defects. The probability distribution functions (p.d.f.) are also provided for each fitting.

and 12(d). However, the competing risk distribution provides an improvement compared to the previous results, particularly for the largest defect size. A significant difference between the two distributions is clearly visible when switching from the Gumbel/GEV distribution to the competing risk one. To estimate this difference, the predicted defect size is calculated using the same cumulative frequency F of the largest observed defect, corresponding to a value of $-\log(-\log(F))=3.2$. For the same value of cumulative frequency F, the predicted defect size increases by 31% from 309 μm to 405 μm, while the observed defects size is at 444 μm.

The residuals of the fittings are computed and associated to the estimated p.d.f. and standard deviations in Fig. 13. These residuals correspond to the difference between the observed defect size and the predicted one at the same probability of occurrence normalized by the predicted defect size. If the data are properly fitted, one would expect the residuals to be normally distributed with centered and symmetrical values. The residuals obtained from the Gumbel distribution of the overall defects highlight the significant inaccuracy of this fitting because a large standard deviation is found (0.16), as shown in Fig. 13(a). The adoption of GEV fitting of the same defect distribution in Fig. 13(b) have a narrow range of residuals, resulting in a lower standard deviation at 0.10 but still a significantly high residual value for the largest defect at approximately 0.5. In Fig. 13(c), the spherical distribution is properly fitted by the proposed Gumbel distribution with a standard deviation of 0.06. Conversely, the fitting on the elongated

defects shows a dis-symmetric distribution resulting in a quite large standard deviation at 0.14, despite the fact that the residual associated with the largest defect was reduced by half at 0.25. Only the use of the competing risk distribution function in Fig. 13(d) leads to a centered and symmetric distribution with a small standard deviation of 0.06. A good prediction of the largest defect size residual is found with a value of 0.12, i.e., +12% of the predicted defect size. The competing risk analysis is the most effective way to describe the distribution of defect sizes, especially in the range of large defects, and it is used to assess the fatigue performance of the material.

In order to verify that the analysis with different populations of defects was not affected by the selection of the investigated volume, the largest defects from the six volumes V_1 were compared with the data obtained and analyzed from volumes V_0. In each of the six investigated volumes V_1, the largest defects were acquired as spherical and elongated discontinuity, providing two separated populations: six maxima spherical defects and six maxima elongated defects. By adopting the "return period" concept as expressed by Eq. (5) the population of defect obtained on V_0 were scaled up to the larger volume V_1. Fig. 14(a) shows that the defects with the corresponding fittings on V_0 exhibited similar statistics when they are scaled up and compared to the separated population of maxima defects observed in the investigated volume V_1. Particularly, the adoption of a smaller volume, such as V_0, has enabled to provide more statistics and it is preferable when
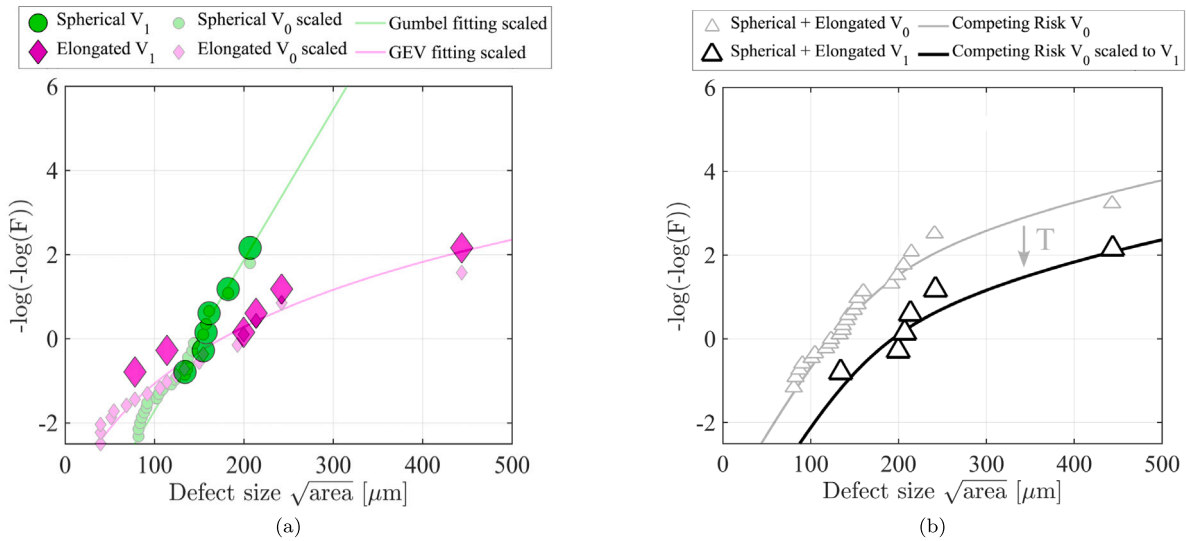
Fig. 14. Influence of the investigated volumes V_0 and V_1 for X-ray data using extreme statistics: (a) effect on spherical and elongated data; (b) competing risk for volume V_0 obtained by the related experimental defects and calculated competing risk for V_1 compared to the six overall largest defects (Spherical+Elongated) in V_1.

there is a limited availability of the acquired data, as in the case of the investigated volume V_1.

Similarly, the competing risk distribution obtained from the investigated volumes V_0 was scaled up to the larger volume V_1 and compared to the six overall largest defects (Spherical+Elongated) measured on V_1. In Fig. 14(b), the competing risk on V_1 (black thick line) was obtained by shifting the competing risk distribution on V_0 (transparent thin line) according to the return period. The transition between the two competing risk distribution is governed by Eq. (5). The obtained distribution representing the welded volume (V_1) describes well the six overall largest defects (Spherical+Elongated) detected on the investigated volume V_1, as shown by Fig. 14(b).

3.2. Fatigue limit estimation

During different operating conditions, such as a start-up, speed no load, maximum opening, and stop, the runner experiences wide range of loading conditions, influencing the load ratio R [11]. For this reason, the fatigue limit was evaluated considering three representative load ratios: R=−1, 0.1 and 0.7.

The fatigue limit was estimated relatively to the defect-free fatigue limit $\Delta\sigma_{w0}$ which is generally set as the stabilized fatigue stress associated with a strain-controlled value of 0.05% at R=−1 [42,46] denoted as $\Delta\sigma_{w0}^{R=-1}$. In the absence of such experimental value, $\Delta\sigma_{w0}$ is usually approximated considering the standard tensile properties of the material. In the present case, as the material undergoes dynamic strain softening, the $\Delta\sigma_{w0}$ value was set at 80% of the σ_{UTS}, i.e., 691 MPa [47]. The dependence of $\Delta\sigma_{w0}$ on R was obtained by using the Goodman equation reported in Eq. (7) [47].

On the other hand, long crack threshold SIF ranges ($\Delta K_{th,LC}$) were already documented in literature for various load ratio R (Table 3) and these values were fitted with NASGRO equation [45] to obtain a $\Delta K_{th,LC}(R)$ function, as illustrated in Fig. 15.

In order to estimate the fatigue limit, the El-Haddad curves were computed for each of the mentioned load ratio R and used to assess the reduction of the fatigue limit stress range ($\Delta\sigma_w$) from its defect-free condition ($\Delta\sigma_{w0}$), represented by $\Delta\sigma_w$ at $\sqrt{area} = 1$ μm. The El-Haddad curves alongside with the p.d.f. of the competing risk distributions are illustrated in Fig. 16 for the three investigated volumes: V_0, V_1, and $V_{HSV}^{80\%}$. These distributions highlight the probability of the defect sizes to fall within a particular range of values. The defect size adopted as $\sqrt{area}$ parameter was in accordance with the definition discussed in
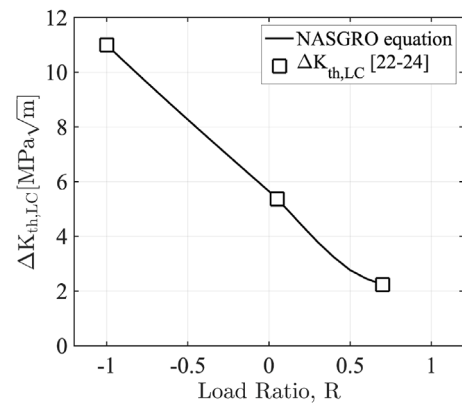

Fig. 15. NASGRO fitting considering $\Delta K_{th,LC}$ presented in Table 3.

Section 2.3.1. As the volume increases, the competing risk distribution shifts to the right with a decrease in the p.d.f. intensity of the mode, illustrating how for larger volumes a wider dispersion is obtained. Characteristic defect sizes for V_0, V_1, and $V_{HSV}^{80\%}$ volumes were computed based on the 90% percentile of their distributions, which correspond to p.d.f. values of approximately 0.0009 for V_0 and 0.0005 for both V_1, and $V_{HSV}^{80\%}$. The 90% percentile was chosen because it focuses on the largest defect sizes, representing the tail end of the distribution. Nevertheless, the provided distribution parameters (Table 7) and the return period T allows plotting the c.d.f. of the competing risk distribution and calculating the defect size corresponding to the desired percentile. The resulting sizes of the defects were 266 μm, 477 μm, and 441 μm for V_0, V_1, and $V_{HSV}^{80\%}$, respectively. The computed defect sizes were then introduced into Eq. (6b) to estimate the associated fatigue limits. A parallel research activity, focused on the defects that control the failure in this material, have shown that similar sizes of defect were critical under cyclic loading. The experimental data are illustrated in Fig. 16 using a boxplot layout, and they refer to a volume of approximately 1350 mm³, representing the reduced section of a standard axial fatigue specimen.

The fatigue limit stress range ($\Delta\sigma_w$) is strongly influenced by load ratio R, as illustrated in Fig. 16. For V_0 the estimation of $\Delta\sigma_w$ at R=0.1 shows a decrease of approximately 45% compared to R=−1 and a 75% decrease at R=0.7. Similar values are found for V_1 and $V_{HSV}^{80\%}$, with a
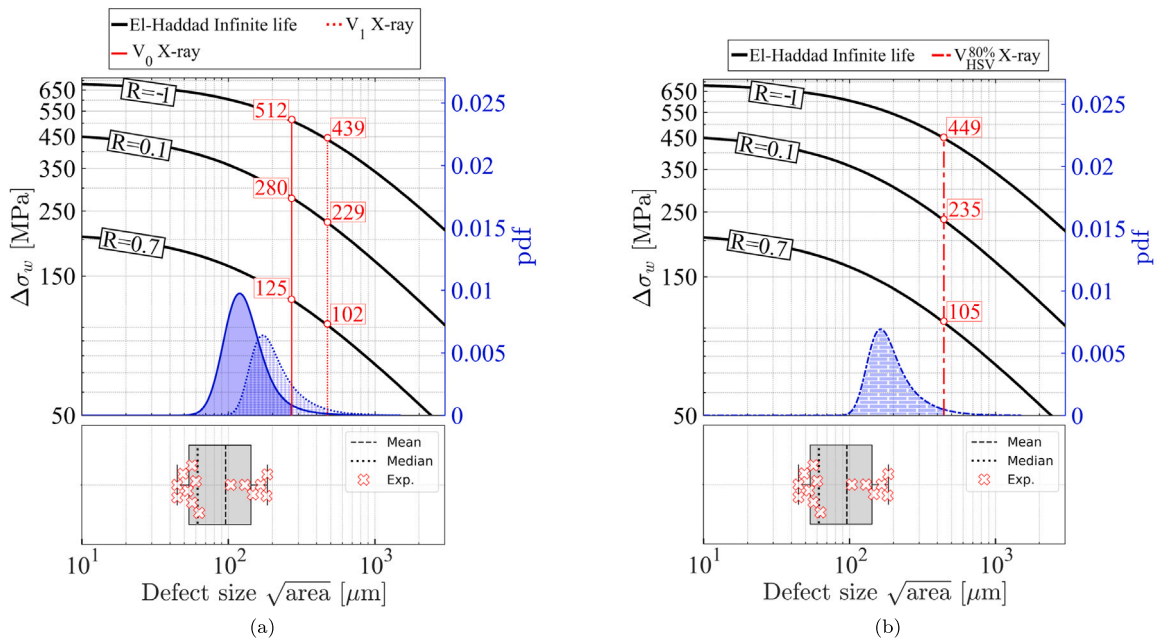
Fig. 16. X-ray results: El-Haddad approximation presented alongside the 90% percentile of the competing risk distribution for load ratios R=−1, 0.1 and 0.7. (a) KT diagram for control volume V_0 and V_1; (b) KT diagram for control volume $V_{HSV}^{80\%}$. The boxplot at bottom of the KT diagram in (a) and (b) represents the experimental defect size controlling the failure for a volume of approximately 1350 mm^3 (reduced section of axial fatigue specimen).

48% decrease of $\Delta\sigma_w$ at R=0.1 compared to R=−1 and a 77% decrease at R=0.7. At constant load ratio R in Fig. 16(a), $\Delta\sigma_w$ decreases as the volume increases from V_0 to V_1 with a drop of 15%, 18%, and 18% for load ratio R of −1, 0.1, and 0.7, respectively. The $\Delta\sigma_w$ estimates for $V_{HSV}^{80\%}$ in Fig. 16(b) are marginally higher (about 3%) to those calculated for V_1 as the associated characteristic defect of $V_{HSV}^{80\%}$ is slightly smaller than V_1 (about 8%).

A parallel procedure was implemented to compute the fatigue performance using the metallographic observations, mirroring the methodology detailed for X-ray data. The competing risk approach was able to fit rather well the defects detected on the 24 available surface areas of 175 mm^2. As discussed in Section 2.3.2, the Murakami approach [7,34] and the equivalent volumes (V_0^*, V_1^*) were determined by multiplying the respective surface area by the average size of the largest defect size observed on the analyzed surface areas. The average defect size calculation has led to fictitious thicknesses h_0=0.087 mm and h_1=0.148 mm. This calculation has provided volumes of 15 mm^3 and 104 mm^3 for V_0^* and V_1^*, respectively. On the other hand, $V_{HSV}^{80\%}$ was kept the same at 1700 mm^3 as it represents the volume of interest for design purposes.

To quantify better the difference between the two methods, a discrepancy of fatigue limits in terms of percentage was calculated and reported in Fig. 17: the metallographic fatigue limit estimation was subtracted to the X-ray fatigue limit estimation and this difference was divided by the X-ray one. The difference between the two methods of acquisition significantly varies from +10% to −79%. Particularly, for smaller volume (V_0^*, V_0) the prediction of the fatigue limit stress range ($\Delta\sigma_w$) through metallographic macro-graphs leads to estimates less conservative than X-ray ones with a discrepancy limited to an overestimation of +10% difference. Conversely, for large volumes (V_1^*, V_1) $\Delta\sigma_w$ metallographic estimates are more conservative than X-ray ones with a discrepancy limited to an underestimation of −27%. This difference becomes overly conservative when considering the investigated volume $V_{HSV}^{80\%}$ with a discrepancy reaching an underestimation of −79% difference, highlighting a fundamental divergence between the two approaches. The discrepancy can be related with the return period associated with the estimation method.

In the case of metallography, the obtained p.d.f. of the competing risk distributions together with the El-Haddad curves is illustrated in
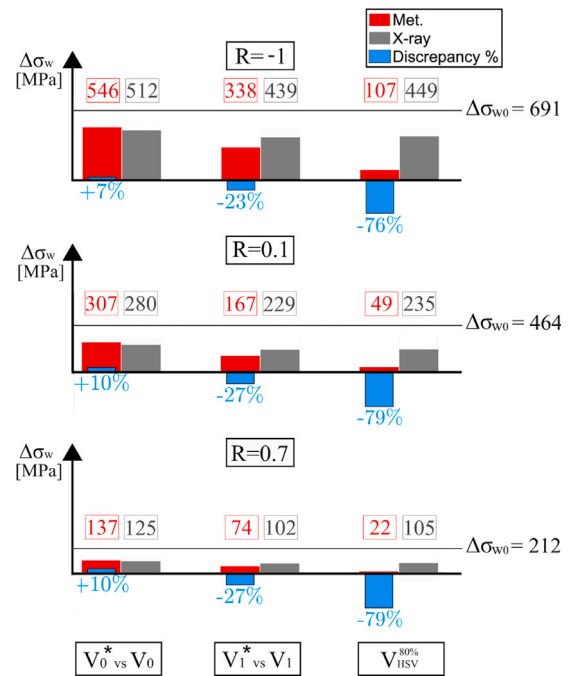

Fig. 17. Fatigue limit estimates $\Delta\sigma_w$ using X-ray and metallography at R=−1,0.1 and 0.7, highlighting discrepancies percentage and defect-free fatigue limit range $\Delta\sigma_{w0}$.

Fig. 18 for the three investigated volumes (V_0^*, V_1^*, and $V_{HSV}^{80\%}$). The 90% percentile of the competing risk distribution for V_0^* has provided a characteristic defects size which is 195 μm corresponding to a p.d.f. value of approximately 0.0007. The resulting characteristic defect size was 27% smaller than the one found for X-ray observation, highlighting the tendency of metallography to detect smaller sizes. The return period between V_1^*, V_0^* is equal to $T_1^* = 6.9$, about 70% higher than the one observed in the X-ray analysis. The increase in the return period was
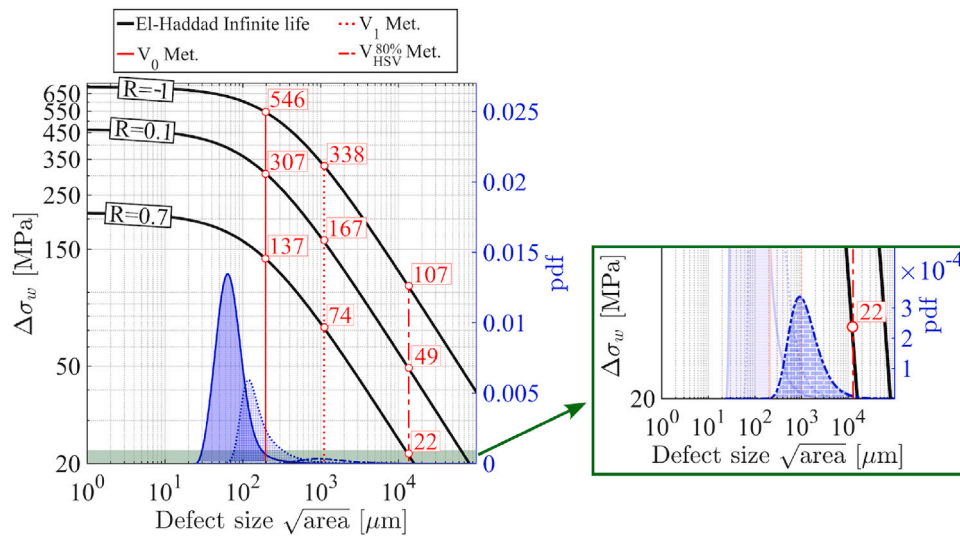
Fig. 18. Metallography results: El-Haddad approximation presented alongside the 90% percentile of the competing risk distributions for the investigated volumes V_0^*, V_1^*, and $V_{HSV}^{80\%}$ at R=−1, 0.1 and 0.7.

caused by the associated fictitious thicknesses ($h_1/h_0 = 1.7$) as the surface areas ratio ($S_1/S_0 = 4$) matches the volumes ratio in the X-ray analysis ($V_1/V_0 = 4$). This large return period moves the V_0^* distribution to the right, resulting in V_1^* competing risk distribution with a value of maximum p.d.f. and mode location close to the V_1 distribution, computed in the X-ray analysis. The approach seems to work if the defect size corresponding to the mode is chosen; however, in terms of extreme values, the increase in the return period results in much larger defect size prediction and significantly lower $\Delta\sigma_w$ estimation. Particularly, the competing risk distribution for V_1^* corresponding to 90% percentile has led to a characteristic defects size of 1025 µm with p.d.f. value of approximately 0.0001. The determined characteristic defect size was about 2.14 times larger than the one obtained in the X-ray analysis. The small number of large defects in the material leads to rather small values for the fictitious thicknesses (h_0, h_1), resulting in equivalent volumes too small compared to the ones associated with X-ray. The fact that large defects were too rare to be captured with metallography in their entirety, has limited the correct estimation of the fictitious thicknesses. The issue becomes even more problematic when computing the competing risk distribution for the volume $V_{HSV}^{80\%}$; the equivalent volume V_0^* is significantly smaller than $V_{HSV}^{80\%}$ (1700 mm³), resulting in a return period as large as 113, approximately 34 times the one observed for the X-ray analysis ($T_{HSV} = 3.3$). Competing risk distribution for $V_{HSV}^{80\%}$ corresponding to 90% percentile has provided a characteristic defect size extremely large at 13250 µm with a very low value of p.d.f. at approximately $5 \cdot 10^{-5}$. The determined characteristic defect size was incredibly larger than the one obtained in the X-ray analysis, showing again that the return period cannot be estimated with the mentioned approach.

In order to achieve consistent $\Delta\sigma_w$ estimations between X-ray and metallography, the characteristic defect size representing the extreme defect and identified by the 90% percentile of the competing risk distribution should have similar value for both methods. In other words, it is possible to define a proper return period so that the metallography results would estimate properly the extreme defect size in the volume of interest ($V_{HSV}^{80\%}$). The value of the return period necessary for this match is equal to $\overline{T}_{HSV} = 2.65$ which defines the expected fictitious thickness to be equal to $\overline{h}_0 = 3.66$ mm as the surface area S_0 is known. The computed fictitious thickness h_0 was 42 times the one considered for the metallography analysis ($h_0 = 0.087$ mm), a value that was not possible to estimate from the metallographic data. Therefore, the proposed method based on metallography data cannot be used to properly estimate the fatigue limit.

It should be highlighted that the hypothesis that the estimated defects from X-ray can predict fatigue performance will have to be validated by a comprehensive fatigue experimental test campaign. In this campaign, fatigue specimens will be scanned using X-ray and then subjected to fatigue testing. This process will provide the insights about the main features of the defects which lead to the fatal failure of the material. The authors will present the results of such fatigue campaign in an upcoming article.

4. Conclusions

The present study proposes methodology to implement Extreme Value Statistics (EVS) to investigate and predict the distribution of defects and the largest characteristic defect size in target volumes for a 13%Cr–4%Ni multi-pass welded material in order to estimate the fatigue properties. Defects in T-shape joint specimens produced by multi-pass welding are documented through both metallographic and 2D X-ray analyses. The dimension of the defects measured in terms of $\sqrt{\text{area}}$ parameter was used to estimate the reduction in fatigue strength using the Kitagawa–Takahashi (KT) diagram with the El-Haddad formulation. Based on the results obtained, the following conclusion can be drawn:

- The competing risk approach improves the prediction of the defect distribution compared to using a Generalized Extreme Value (GEV) and Gumbel distributions on all data set. It is recommended to classify the defect population in terms of geometry to avoid inconsistent analyses;
- The distribution of defects in 13%Cr–4%Ni multi-pass welded material was divided in two populations based on their geometry (spherical and elongated discontinuities);
- The competing risk approach improves the prediction of the defect distribution compared to using a Generalized Extreme Value (GEV) and Gumbel distributions on all data set. It is then recommended to classify the defect population in terms of geometry to improve the statistical analysis;
- By the separated fitting of spherical and elongated discontinuities, it was shown that the wrong population of defects can be characterized if the size of the analyzed volume is not large enough;
- Metallography offers greater precision in terms of defect morphology but provides limited information as it cannot capture defects below the observation plane and no realistic volume can be associated with the observed data for further statistical prediction. Conversely, X-ray analysis provides more comprehensive

information as it can penetrate through the material and it can be associate without ambiguity to a specific volume;

- Defects acquired with X-ray and metallographic measurements have evidenced a significant difference in terms of fatigue limit estimations, highlighting the necessity to adopt a discrepancy factor between the two methods of acquisition;
- The results have shown that metallographic statistical analysis might generate inaccurate fatigue assessment due to large return periods resulting into wider dispersion of the defect size;
- The estimated fatigue limit stress ranges $\Delta\sigma_w$ were presented for different load ratios, providing typical stress values to perform a fatigue test campaign and to design components made of multi-pass welds with specific material and welding conditions.

CRediT authorship contribution statement

Declaration of competing interest

The authors declare the following financial interests/personal relationships which may be considered as potential competing interests: Antonio D'Andrea reports financial support was provided by Hydro-Quebec's Research Institute. Antonio D'Andrea reports financial support was provided by Natural Sciences and Engineering Research Council of Canada. Antonio D'Andrea reports a relationship with Sacmi Imola SC that includes: funding grants. If there are other authors, they declare that they have no known competing financial interests or personal relationships that could have appeared to influence the work reported in this paper.

Data availability

The data that has been used are confidential.

Acknowledgments

References

[1] Davydov A, Alekseeva E, Kolnyshenko V, Strekalovskaya D, Shvetsov O, Devyaterikova N, Laev K, Alkhimenko A. Corrosion resistance of 13Cr steels. Metals 2023;13(11):1805. http://dx.doi.org/10.3390/met13111805, URL https://www.mdpi.com/2075-4701/13/11/1805.

[2] Gagnon M, Tahan SA, Bocher P, Thibault D. Impact of startup scheme on Francis runner life expectancy. Inst Phys Publ (IOP) 2010;12:012107. http://dx.doi.org/10.1088/1755-1315/12/1/012107, URL https://iopscience.iop.org/article/10.1088/1755-1315/12/1/012107.

[3] Zhu D, Tao R, Xiao R, Pan L. Solving the runner blade crack problem for a Francis hydro-turbine operating under condition-complexity. Renew Energy 2020;149:298–320. http://dx.doi.org/10.1016/j.renene.2019.12.057, URL https://linkinghub.elsevier.com/retrieve/pii/S0960148119319299.

[4] Liu X, Luo Y, Wang Z. A review on fatigue damage mechanism in hydro turbines. Renew Sustain Energy Rev 2016;54:1–14. http://dx.doi.org/10.1016/j.rser.2015.09.025, URL https://linkinghub.elsevier.com/retrieve/pii/S1364032115009958.

[5] Boukani HH, Viens M, Tahan S-A, Gagnon M. Case study on the integrity and nondestructive inspection of flux-cored arc welded joints of Francis turbine runners. Int J Adv Manuf Technol 2018;98(5–8):2201–11. http://dx.doi.org/10.1007/s00170-018-2139-y, URL http://link.springer.com/10.1007/s00170-018-2139-y.

[6] Bajgholi ME, Rousseau G, Viens M, Thibault D. Capability of advanced ultrasonic inspection technologies for hydraulic turbine runners. Appl Sci 2021;11(10):4681. http://dx.doi.org/10.3390/app11104681, URL https://www.mdpi.com/2076-3417/11/10/4681.

[7] Murakami Y. Effects of nonmetallic inclusions on fatigue strength. In: Metal fatigue: effects of small defects and nonmetallic inclusions. Elsevier; 2019, p. 95–150. http://dx.doi.org/10.1016/B978-0-12-813876-2.00006-6, URL https://linkinghub.elsevier.com/retrieve/pii/B9780128138762000066.

[8] Sanaei N, Fatemi A. Defects in additive manufactured metals and their effect on fatigue performance: A state-of-the-art review. Prog Mater Sci 2021;117:100724. http://dx.doi.org/10.1016/j.pmatsci.2020.100724, URL https://linkinghub.elsevier.com/retrieve/pii/S0079642520300888.

[9] Romano S, Nezhadfar PD, Shamsaei N, Seifi M, Beretta S. High cycle fatigue behavior and life prediction for additively manufactured 17-4 PH stainless steel: Effect of sub-surface porosity and surface roughness. Theor Appl Fract Mech 2020;106:102477. http://dx.doi.org/10.1016/j.tafmec.2020.102477, URL https://www.sciencedirect.com/science/article/pii/S0167844219307062.

[10] Romano S, Miccoli S, Beretta S. A new FE post-processor for probabilistic fatigue assessment in the presence of defects and its application to AM parts. Int J Fatigue 2019;125:324–41. http://dx.doi.org/10.1016/j.ijfatigue.2019.04.008, URL https://www.sciencedirect.com/science/article/pii/S014211231930132X.

[11] Gagnon M, Tahan A, Bocher P, Thibault D. A probabilistic model for the onset of high cycle fatigue (HCF) crack propagation: Application to hydroelectric turbine runner. Int J Fatigue 2013;47:300–7. http://dx.doi.org/10.1016/j.ijfatigue.2012.09.011, URL https://linkinghub.elsevier.com/retrieve/pii/S0142112312002757.

[12] Romano S, Brandão A, Gumpinger J, Gschweitl M, Beretta S. Qualification of AM parts: Extreme value statistics applied to tomographic measurements. Mater Des 2017;131:32–48. http://dx.doi.org/10.1016/j.matdes.2017.05.091, URL https://www.sciencedirect.com/science/article/pii/S0264127517305737.

[13] Reiss R-D, Thomas M. Statistical analysis of extreme values: with applications to insurance, finance, hydrology and other fields. third ed.. Birkhäuser; 2007, URL https://scholar.google.com/scholar_lookup?title=Statistical%20Analysis%20of%20Extreme%20Values&author=R.%20Reiss&publication_year=1997.

[14] Coles S, Bawa J, Trenner L, Dorazio P. An introduction to statistical modeling of extreme values. Vol. 208, Springer; 2001, URL https://scholar.google.ca/scholar?hl=en&as_sdt=0%2C5&as_vis=1&q=An+introduction+to+statistical+modeling+of+extreme+values+coles&btnG=.

[15] Murakami Y. Inclusion rating by statistics of extreme values and its application to fatigue strength prediction and quality control of materials. J Res Natl Inst Stand Technol 1994;99(4):345. http://dx.doi.org/10.6028/jres.099.032, URL https://nvlpubs.nist.gov/nistpubs/jres/099/jresv99n4p345_A1b.pdf.

[16] Kitagawa H. Fracture-mechanics study of the growth of small crack and its threshold.. In: ASM proc. 2nd intern. conf. mech. behav. mater.. 1976, p. 627–31, URL https://www.jstage.jst.go.jp/article/kikaia1979/45/399/45_399_1289/_article/-char/ja/.

[17] Zerbst U, Bruno G, Buffière J-Y, Wegener T, Niendorf T, Wu T, Zhang X, Kashaev N, Meneghetti G, Hrabe N, Madia M, Werner T, Hilgenberg K, Koukolíková M, Procházka R, Džugan J, Möller B, Beretta S, Evans A, Wagener R, Schnabel K. Damage tolerant design of additively manufactured metallic components subjected to cyclic loading: State of the art and challenges. Prog Mater Sci 2021;121:100786. http://dx.doi.org/10.1016/j.pmatsci.2021.100786, URL https://linkinghub.elsevier.com/retrieve/pii/S0079642521000104.

[18] Hu YN, Wu SC, Wu ZK, Zhong XL, Ahmed S, Karabal S, Xiao XH, Zhang HO, Withers PJ. A new approach to correlate the defect population with the fatigue life of selective laser melted Ti-6Al-4V alloy. Int J Fatigue 2020;136:105584. http://dx.doi.org/10.1016/j.ijfatigue.2020.105584, URL https://www.sciencedirect.com/science/article/pii/S0142112320301158.

[19] Chapetti MD. Fracture mechanics for fatigue design of metallic components and small defect assessment. Int J Fatigue 2022;154:106550. http://dx.doi.org/10.1016/j.ijfatigue.2021.106550, URL https://linkinghub.elsevier.com/retrieve/pii/S0142112321004047.

[20] Thibault D, Bocher P, Thomas M, Gharghouri M, Côté M. Residual stress characterization in low transformation temperature 13%Cr–4%Ni stainless steel weld by neutron diffraction and the contour method. Mater Sci Eng A 2010;527(23):6205–10. http://dx.doi.org/10.1016/j.msea.2010.06.035, URL https://linkinghub.elsevier.com/retrieve/pii/S0921509310006684.

[21] Amrei MM, Monajati H, Thibault D, Verreman Y, Bocher P. Effects of various post-weld heat treatments on austenite and carbide formation in a 13Cr4Ni steel multipass weld. Metall Microstruct Anal 2016;5(1):50–61. http://dx.doi.org/10.1007/s13632-015-0251-z, URL http://link.springer.com/10.1007/s13632-015-0251-z.

[22] Tanaka H. Studies on Dynamic Stress of Runners for the Design of 760 Meter Head Pump-turbines. In: International association for hydro-environment engineering and research (IAHR) syposium. 1992, URL https://cir.nii.ac.jp/crid/1573668924862363392.

[23] Usami S, Shida S. Elastic-Plastic analysis of the fatigue limit for a material with small flaws. Fatigue Fract Eng Mater Struct 1979;1(4):471–81. http://dx.doi.org/10.1111/j.1460-2695.1979.tb01334.x, URL https://onlinelibrary.wiley.com/doi/10.1111/j.1460-2695.1979.tb01334.x.

[24] Usami S, Shida S. Effects of environment, stress ratio and defect size on fatigue threshold. J Soc Mater Sci 1982;31(344):493–9. http://dx.doi.org/10.2472/jsms.31.493.

[25] Thumser R, Kleemann S, Bergmann JW, Kleemann A. Investigation on defect distribution and its statistical evaluation for case hardened material states. Int J Fatigue 2012;41:52–6. http://dx.doi.org/10.1016/j.ijfatigue.2012.01.024, URL https://linkinghub.elsevier.com/retrieve/pii/S0142112312000412.

[26] Romano S, Abel A, Gumpinger J, Brandão AD, Beretta S. Quality control of AlSi10Mg produced by SLM: Metallography versus CT scans for critical defect size assessment. Addit Manuf 2019;28:394–405. http://dx.doi.org/10.1016/j.addma.2019.05.017, URL https://www.sciencedirect.com/science/article/pii/S2214860419302052.

[27] Meimandi S, Vanderesse N, Thibault D, Bocher P, Viens M. Macro-defects characterization in cast CA-6NM martensitic stainless steel. Mater Charact 2017;124:31–9. http://dx.doi.org/10.1016/j.matchar.2016.11.040, URL https://linkinghub.elsevier.com/retrieve/pii/S1044580316310725.

[28] Chávez J, Valencia J, Jaramillo G, Coronado J, Rodríguez S. Failure analysis of a Pelton impeller. Eng Fail Anal 2015;48:297–307. http://dx.doi.org/10.1016/j.engfailanal.2014.08.012, URL https://linkinghub.elsevier.com/retrieve/pii/S1350630714002738.

[29] Schindelin J, Arganda-Carreras I, Frise E, Kaynig V, Longair M, Pietzsch T, Preibisch S, Rueden C, Saalfeld S, Schmid B, Tinevez J-Y, White DJ, Hartenstein V, Eliceiri K, Tomancak P, Cardona A. Fiji: an open-source platform for biological-image analysis. Nat Methods 2012;9(7):676–82. http://dx.doi.org/10.1038/nmeth.2019, URL http://dx.doi.org/10.1038/nmeth.2019.

[30] Vander Voort GF, Lucas GM, Manilova EP. Metallography and Microstructures of Stainless Steels and Maraging Steels. Metall Microstruct ASM Int 2004. URL http://dx.doi.org/10.31399/asm.hb.v09.a0003767.

[31] Amrei MM, Monajati H, Thibault D, Verreman Y, Germain L, Bocher P. Microstructure characterization and hardness distribution of 13Cr4Ni multipass weld metal. Mater Charact 2016;111:128–36. http://dx.doi.org/10.1016/j.matchar.2015.11.022, URL https://linkinghub.elsevier.com/retrieve/pii/S1044580315300620.

[32] Sanaei N, Fatemi A, Phan N. Defect characteristics and analysis of their variability in metal L-PBF additive manufacturing. Mater Des 2019;182:108091. http://dx.doi.org/10.1016/j.matdes.2019.108091, URL https://linkinghub.elsevier.com/retrieve/pii/S0264127519305295.

[33] Beretta S. More than 25 years of extreme value statistics for defects: Fundamentals, historical developments, recent applications. Int J Fatigue 2021;151:106407. http://dx.doi.org/10.1016/j.ijfatigue.2021.106407, URL https://www.sciencedirect.com/science/article/pii/S014211232100267X.

[34] Uemura Y, Murakami Y. A numerical simulation of evaluating the maximum size of inclusions to examine the validity of the metallographic determination of the maximum size of inclusions. Trans Japan Soc Mech Eng Ser A 1990;56(521):162–7. http://dx.doi.org/10.1299/kikaia.56.162.

[35] Beretta S, Anderson CW. The challenge of multiple particles in extreme value inclusion rating. J ASTM Int 2006;3(2):8, URL https://compass.astm.org/document/?contentCode=ASTM%7CJAI14041%7Cen-US.

[36] Kuguel R. A Relation Between Theoretical Stress Concentration Factor and Fatigue Notch Factor Deduced from the Concept of Highly Stressed Volume. Vol. 61, ASTM; 1961, p. 732–48, URL https://scholar.google.com/scholar_lookup?title=A%20relation%20between%20theoretical%20stress%20concentration%20factor%20and%20fatigue%20notch%20factor%20deduced%20from%20the%20concept%20of%20highly%20stressed%20volume&author=R.%20Kuguel&publication_year=1961&pages=732-748.

[37] Sonsino CM, Kaufmann H, Grubišić V. Transferability of material data for the example of a randomly loaded forged truck stub axle. SAE Int 1997. http://dx.doi.org/10.4271/970708, URL https://saemobilus.sae.org/content/970708/.

[38] Sonsino C, Kaufmann H, Grubisic V. Übertragbarkeit von werkstoffkennwerten am beispiel eines betriebsfest auszulegenden geschmiedeten Nutzfahrzeug-Achsschenkels. 1995, URL https://publica.fraunhofer.de/h{and}le/publica/187230.

[39] Beretta S, Patriarca L, Gargourimotlagh M, Hardaker A, Brackett D, Salimian M, Gumpinger J, Ghidini T. A benchmark activity on the fatigue life assessment of AlSi10Mg components manufactured by L-PBF. Mater Des 2022;218:110713. http://dx.doi.org/10.1016/j.matdes.2022.110713, URL https://linkinghub.elsevier.com/retrieve/pii/S0264127522003355.

[40] Morissette JF, Nicolle J. Fluid–structure simulations of the stochastic behaviour of a medium head Francis turbine during startup. Inst Phys Publ (IOP) 2019;240:022026. http://dx.doi.org/10.1088/1755-1315/240/2/022026, URL https://iopscience.iop.org/article/10.1088/1755-1315/240/2/022026.

[41] Rigon D, Meneghetti G. Engineering estimation of the fatigue limit of wrought and defective additively manufactured metals for different load ratios. Int J Fatigue 2022;154:106530. http://dx.doi.org/10.1016/j.ijfatigue.2021.106530, URL https://linkinghub.elsevier.com/retrieve/pii/S0142112321003844.

[42] Haddad MHE, Topper TH, Smith KN. Prediction of non propagating cracks. Eng Fract Mech 1979;11(3):573–84. http://dx.doi.org/10.1016/0013-7944(79)90081-X, URL https://www.sciencedirect.com/science/article/pii/001379447990081X.

[43] Minerva G, Awd M, Tenkamp J, Walther F, Beretta S. Machine learning-assisted extreme value statistics of anomalies in AlSi10Mg manufactured by L-PBF for robust fatigue strength predictions. Mater Des 2023;235:112392. http://dx.doi.org/10.1016/j.matdes.2023.112392, URL https://linkinghub.elsevier.com/retrieve/pii/S0264127523008079.

[44] Patriarca L, Beretta S, Foletti S, Riva A, Parodi S. A probabilistic framework to define the design stress and acceptable defects under combined-cycle fatigue conditions. Eng Fract Mech 2020;224:106784. http://dx.doi.org/10.1016/j.engfracmech.2019.106784, URL https://www.sciencedirect.com/science/article/pii/S001379441930428X.

[45] Maierhofer J, Pippan R, Gänser H-P. Modified NASGRO equation for physically short cracks. Int J Fatigue 2014;59:200–7. http://dx.doi.org/10.1016/j.ijfatigue.2013.08.019, URL https://linkinghub.elsevier.com/retrieve/pii/S014211231300234X.

[46] Sausto F, Carrion P, Shamsaei N, Beretta S. Fatigue failure mechanisms for AlSi10Mg manufactured by L-PBF under axial and torsional loads: The role of defects and residual stresses. Int J Fatigue 2022;162:106903. http://dx.doi.org/10.1016/j.ijfatigue.2022.106903, URL https://linkinghub.elsevier.com/retrieve/pii/S0142112322001736.

[47] Dowling N. mechanical behaviour of materials. engineering methods for deformation, fracture, and fatigue. fourth ed.. Pearson Education Limited; 2013, URL https://scholar.google.com/scholar_lookup?title=Mechanical%20behavior%20of%20materials%3A%20Engineering%20methods%20for%20deformation%2C%20fracture%2C%20and%20fatigue%2C%20fourth%20edition&author=N.E.%20Dowling&publication_year=2013.